

A metamaterial scaffold beyond modulus limits: enhanced osteogenesis and angiogenesis of critical bone defects

Received: 3 May 2024

Accepted: 20 February 2025

Published online: 04 March 2025

Yu Qin^{1,2,3,6}, Zehao Jing^{2,3,6}, Da Zou^{2,3}, Youhao Wang^{2,3}, Hongtao Yang⁴, Kai Chen¹, Weishi Li^{2,3}✉, Peng Wen⁵✉ & Yufeng Zheng¹✉

Metallic scaffolds have shown promise in regenerating critical bone defects. However, limitations persist in achieving a modulus below 100 MPa due to insufficient strength. Consequently, the osteogenic impact of lower modulus and greater bone tissue strain ($>1\%$) remains unclear. Here, we introduce a metamaterial scaffold that decouples strength and modulus through two-stage deformation. The scaffold facilitates an effective modulus of only 13 MPa, ensuring adaptability during bone regeneration. Followed by a stiff stage, it provides the necessary strength for load-bearing requirements. In vivo, the scaffold induces $>2\%$ callus strain, upregulating calcium channels and HIF-1 α to enhance osteogenesis and angiogenesis. 4-week histomorphology reveals a 44% and 498% increase in new bone fraction versus classic scaffolds with 500 MPa and 13 MPa modulus, respectively. This design transcends traditional modulus-matching paradigms, prioritizing bone tissue strain requirements. Its tunable mechanical properties also present promising implications for advancing osteogenesis mechanisms and addressing clinical challenges.

Despite bones' regenerative prowess, the suboptimal reconstruction of critical bone defects, frequently caused by infections, tumors, and trauma, remains a significant clinical concern¹. The predominant treatment involves total endoprosthetic replacement using metallic implants, especially in load-bearing bones. However, commonly used implant metals, including titanium and its alloys, exhibit elastic moduli (approximately 110 GPa) that are significantly higher than that of natural bone (0.2–2 GPa for trabecular bone; 3–30 GPa for compact bone)². As a result, during loading, the majority of the stress is borne by the metal, leading to strain shielding and impaired reconstruction of the bone tissue as described by Wolff's law³. 3D printed scaffolds can effectively reduce the modulus of metal implants, meanwhile provide a customized geometrical shape and internal pores that facilitate nutrient delivery and promote bone tissue growth⁴. Classical scaffold

design paradigm emphasizes matching the modulus of the bone^{2,5}, which is intrinsically designed to produce sufficient strain on the surrounding bone tissue during stresses. Pobloth et al. designed scaffolds with varying moduli for treating critical bone defects. They determined the minimum-modulus scaffold of 840 MPa has optimized endochondral and intramembranous ossification, due to a maximum strain of surrounding callus tissue up to 0.6%⁶. While theoretical simulations suggest that 0.23–5% callus tissue strains promote bone regeneration^{7,8}, tissue strains greater than 1% has been regarded unattainable in vivo, and whether such great strain can effectively promote bone regeneration remains unknown. The main challenge lies in the lower limit of the scaffold strength. Conventionally designed scaffolds typically exhibit a strong coupling effect between modulus and strength. Notably, for common titanium scaffolds, achieving a

¹School of Materials Science and Engineering, Peking University, Beijing, China. ²Department of Orthopedics, Peking University Third Hospital, Beijing, China.³Engineering Research Center of Bone and Joint Precision Medicine, Ministry of Education, Peking University Third Hospital, Beijing, China. ⁴School of Biological Science and Medical Engineering, Beihang University, Beijing, China. ⁵Department of Mechanical Engineering, Tsinghua University, Beijing, China.⁶These authors contributed equally: Yu Qin, Zehao Jing. ✉e-mail: puh3liweishi@163.com; wenpeng@tsinghua.edu.cn; yfzheng@pku.edu.cn

modulus below 500 MPa usually requires a porosity above 90%, resulting in a strength of only 10 MPa⁹. Persistently reducing the scaffold modulus diminishes its strength, thereby bringing about fixation failure¹⁰.

The pursuit of low-modulus, high-strength structures¹¹, as well as materials¹², is essential and represents a crucial direction in current bone implant research. To overcome the mechanical limitations of existing materials, mechanical metamaterials leverage the rational design of their microstructures to achieve unique and programmable mechanical properties, such as corrugated¹³, chiral¹⁴, and auxetic materials¹⁵. The limited studies on metamaterial bone implants primarily focused on auxetic materials^{16,17}. For instance, auxetic metamaterials were employed in spinal fusion for monitoring bone healing progress¹⁸. Additionally, the auxetic properties can enhance the pull-out resistance of bone screws¹⁹. Nevertheless, no significant benefits in promoting bone regeneration have been demonstrated since the existing researches on metamaterial scaffolds did not fully consider bone biomechanics. Here, we introduce a two-stage metamaterial scaffold (TMS) for critical bone defects (Fig. 1a). The scaffolds are additively manufactured with electron beam powder bed fusion (EBPBF) (Fig. 1b and Fig. S1). Such an innovative design aims to decouple the modulus and strength of the scaffold so that low modulus and high strength are achieved according to bone repairing needs. Specifically, under primary stress conditions (10 N, 1/3 of the experimental animal's weight), the TMS operates in the ductile stage, showcasing a low modulus of 13 MPa and enabling sufficient strain (>1%). Under extreme conditions (60 N, 2 times the experimental animal's weight), TMS reaches the stiff stage and demonstrates

adequate strength without a significant increase in strain (Fig. 1c). After in vivo implantation (Fig. 1d), The TMS exhibits a robust capacity to promote bone regeneration compared to two classic scaffolds with moduli of 500 MPa (CS) and 13 MPa (CS2), respectively. Therefore, this study demonstrates the two-stage scaffold's capability to maintain appropriate tissue strain while providing sufficient strength to address challenging critical bone defects, offering the potential to usher in a new paradigm for bone scaffold design.

Results

Mechanical design and behaviors

To achieve the two-stage mechanical behavior, the TMS is designed with a double helix configuration composed of interconnected springs. Additionally, pillars are introduced to establish a connection between the springs. The design features a variable gap between the springs, denoted as l_g (Fig. 2a and Fig. S2). The springs have a same side length (l_s), while the pillars have a diameter of d_p . At $l_g = 0$, the classic scaffold (CS) with the conventional modulus-matching objective is established. By reducing d_p to 0, another classic scaffold, CS2, was designed (Fig. S3a). Both classic scaffolds served as control groups (Fig. 2a). Compared with CS (Fig. 2b), the TMS exhibits its distinctive two-stage behavior: at the initial stage with strain less than 2.5%, the compressive stress is relatively inconspicuous, while a more significant increase in stress occurs after larger strains are applied (Fig. 2c). To quantitatively describe the compression deformation process, Fig. 2d depicts the magnification of the strain-stress curve within the maximum threshold of strain that promotes bone formation (5%). The CS has a modulus of only 503 MPa, which is within the range of natural

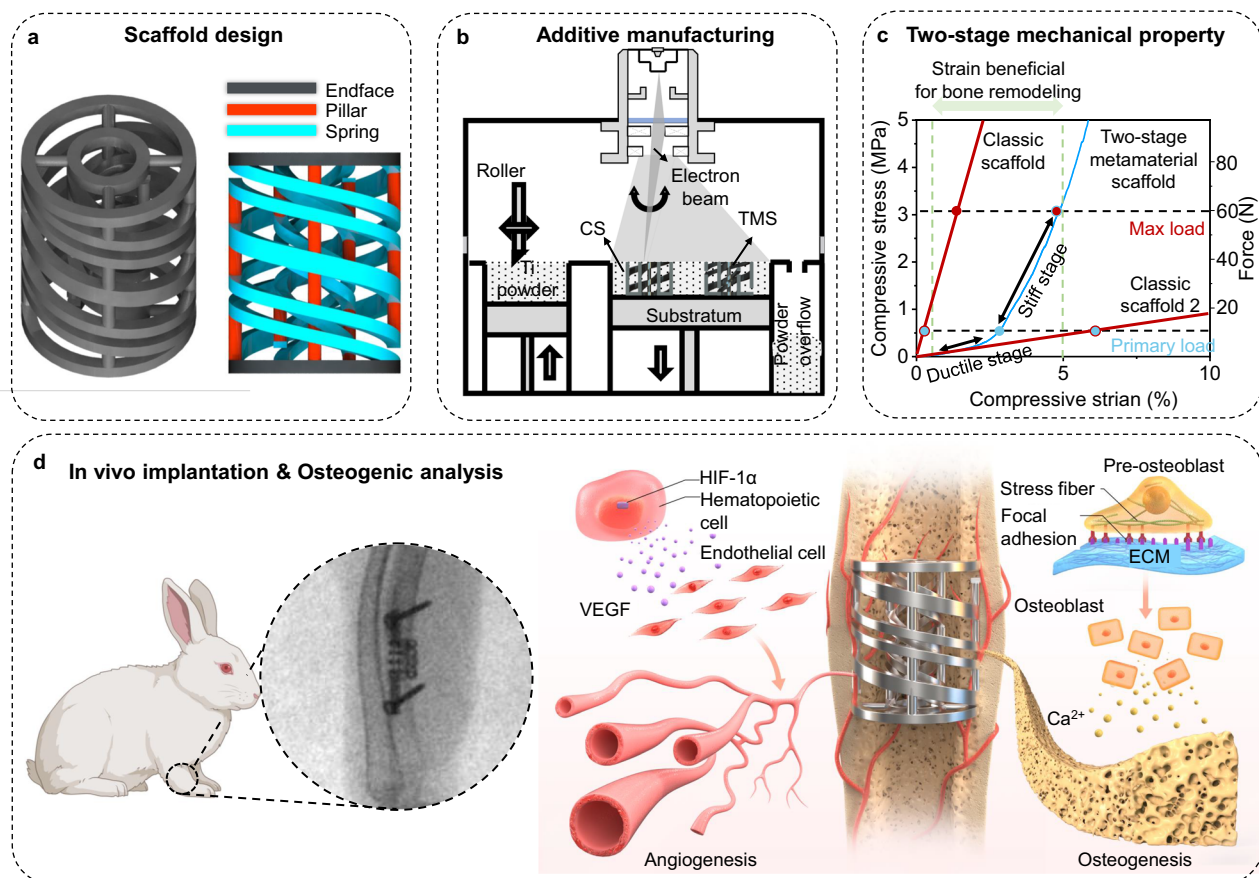


Fig. 1 | Workflow of the proposed metamaterial scaffold. a Structural design of a two-stage metamaterial scaffold (TMS) for critical bone defects. **b** Electron-beam 3D printing technique fabricates the proposed metallic TMS and classic scaffold (CS) design. **c** Mechanical tests demonstrate the two-stage modulus of TMS.

d Afterwards, scaffolds are in vivo implanted in rabbits' critical ulnar defects, and TMS illustrates activation of mechano-biosensors. The upregulation of calcium ion channels and HIF-1α facilitate osteogenesis and angiogenesis. Part of Fig. 1d was created in BioRender. Qin, Y. (2025) <https://BioRender.com/a20k104>.

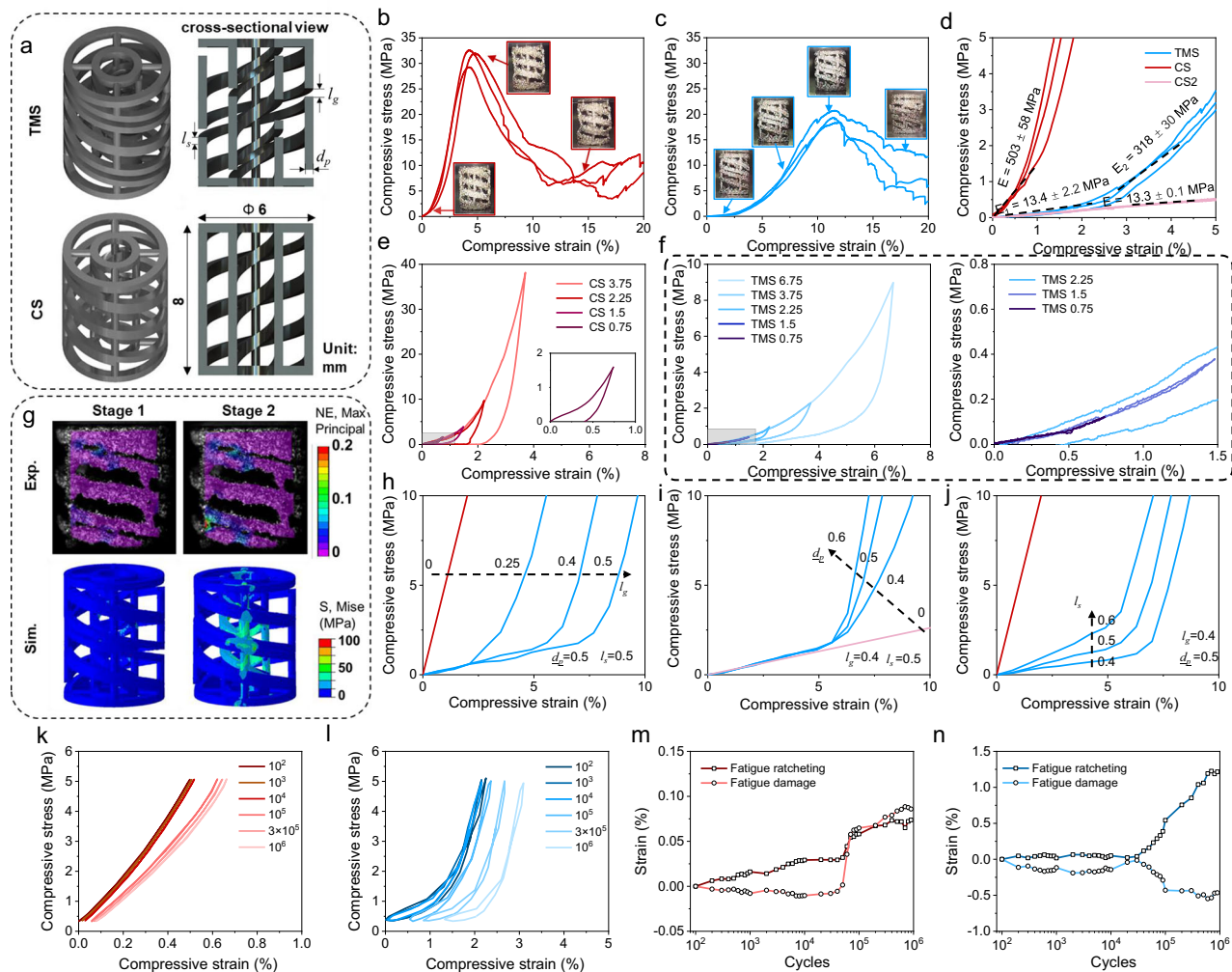


Fig. 2 | Design and mechanical behaviors of TMS and CS. **a** Design parameters of TMS and CS. **b, c** The experimental strain-stress curves ($n = 3$) of the CS and TMS, respectively. **d** Enlarged strain-stress-force curves demonstrate a clear two-stage pattern of TMS with different moduli (E). The modulus is presented as mean \pm SD ($n = 3$). Load-unload behaviors: **e** CS shows strong hysteresis when compressed to a strain of 0.75, 1.5, 2.25 and 3.75%, respectively. **f** TMS holds complete resilience with a maximum compressive strain of 1.5%. **g** Digital image correlation (DIC) calculated

max principal of nominal strain (NE) and simulated von-mise stress of TMS compression. **h–j** The simulated strain-stress curves with changing design parameters: **(h)** l_g , **(i)** d_p and **(j)** l_s . The red lines represent CS when $l_g = 0$. The pink lines represent CS2 when $d_p = 0$. Blue lines represent TMS. **k, l** hysteresis loops shift along the strain axis: **(k)** CS, and **(l)** TMS. **m, n** Calculation of fatigue ratcheting and fatigue damage strains.

bone and near the minimum modulus of Ti scaffolds for force-bearing bone implants²⁰. The TMS demonstrates an effective modulus of only 13.4 MPa, producing an inflection point strain of 2.5% with a small force of 10 N. Additional compressive forces result in the stiff stage of the TMS, where the modulus reaches 318 MPa. When subjected to a total force of 60 N (twice the animal's body weight), the strain is still within 5%, demonstrating both strong and elastic capacity. The CS2 lacks a second stiff stage and maintains a modulus of only 13.3 MPa, equivalent to the first-stage modulus of TMS. Even when the compressive strain reaches 40%, the strength of CS2 remains below 2 MPa (Fig. S3b). The results of the three-point bending test (Fig. S4) also revealed the non-linear deformation of TMS, further substantiating its ability to provide sufficient strain under complex loads.

Compression unloading and fatigue tests were also performed to assess the flexibility of the structure. The CS structure was unable to return to its origin after reaching a strain of 0.75%, implying yielding from early compression (Fig. 2e). On the contrary, the TMS is able to fully recover when compressed to a strain of 1.5%, demonstrating excellent resilience (Fig. 2f). To analyze the rationale creation of TMS and its exceptional adaptability, we investigate the deformation characteristics of its compression process using DIC and finite

elements modelling (Fig. 2g). The ductile stage of the TMS structure is mainly deformed by a spring, which ensures excellent flexibility and low modulus. During the compression process, the two springs gradually overlap, thus the force is transferred to the pillars. This leads to the stiff stage, which has a higher modulus and strength. Based on the mechanical deformation physics, the compression of TMS behaviors can also be controlled by modifying the design parameters (Fig. S5). Strain at inflection points can be regulated by changing l_g (Fig. 2h). By augmenting the value of d_p , as Fig. 2i shows, the modulus of the stiff stage underwent an elevation, leading to an improvement in the compression strength. Also, an increase in l_s can lead to an increase in the ductile-stage modulus (Fig. 2j).

Regarding the performance of compression fatigue (Fig. 2k–n and Fig. S6), both TMS and CS demonstrated sufficient redundancy in fatigue properties for in vivo applications, but their fatigue behaviors showed distinctive features. Notably, the TMS structure successfully endured one million compression cycles with a load twice the animal's body weight, and still retained its two-stage characteristics. CS exhibited a sudden increase in fatigue damage after approximately 80,000 cycles. Whereas TMS underwent negative fatigue damage, suggesting a certain work hardening effect during fatigue tests. Meanwhile, TMS

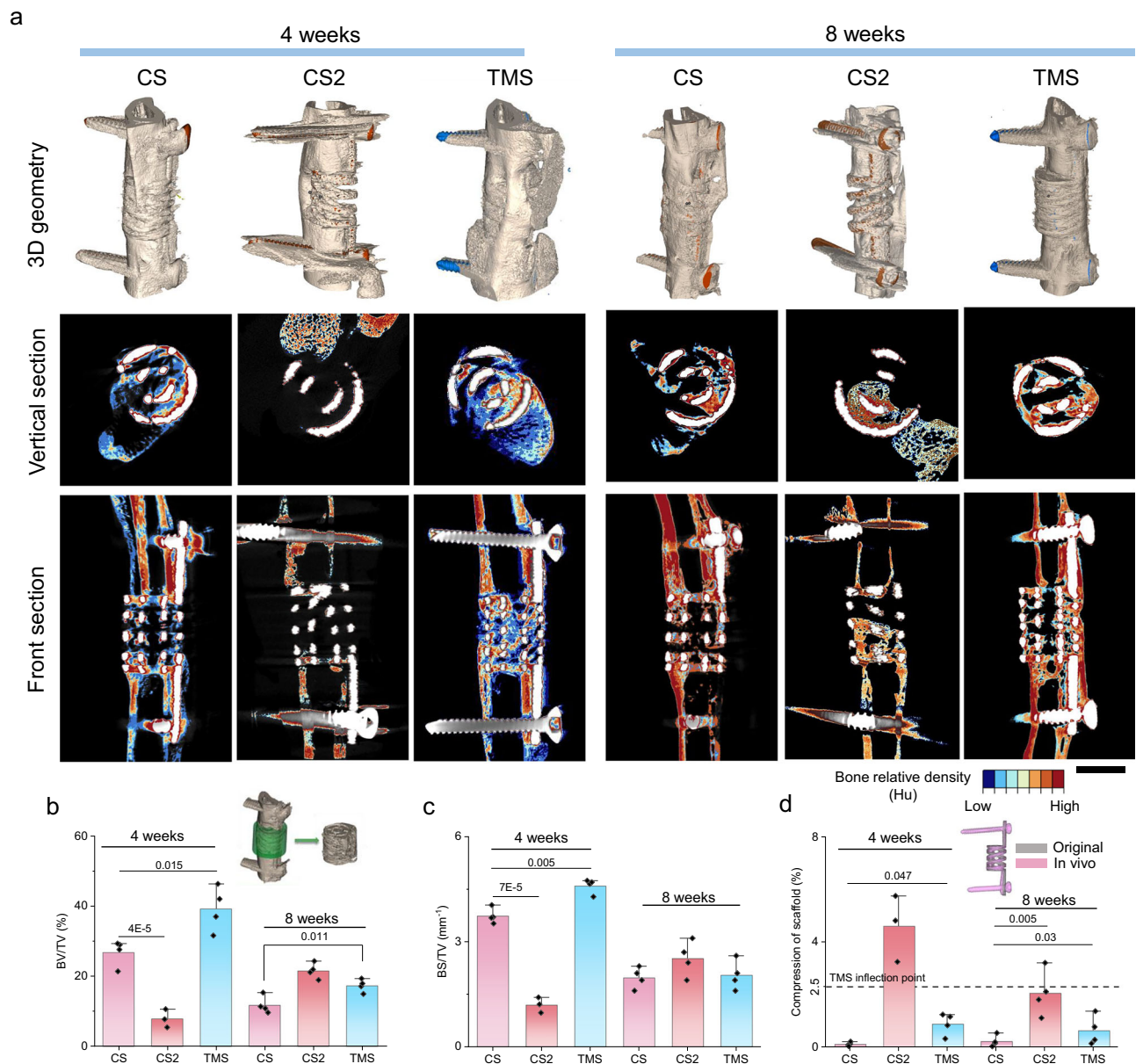


Fig. 3 | TMS enhanced bone regeneration with proper tissue strain. **a** 3D reconstruction of bone regeneration by micro-CT scanning. Cross sections show distinguished parts of scaffolds (bright) and bone relative density heatmap with Hounsfield units (Hu), scale bar = 5 mm. **b, c** Osteogenesis in the green region of interest (ROI) was quantified by two indicators: bone volume/tissue volume

(BV/TV) and bone surface area/ tissue volume (BS/TV). **d** In vivo compression of scaffold calculated from the original (gray) and post-implantation lengths (pink). *p*-value of statistical significance is calculated by one-way ANOVA with Tukey's post hoc test. Data are presented as mean \pm SD. (*n* = 4, except for CS2, where *n* = 3 at 4 weeks due to one instance of mortality).

structure predominantly exhibited ratcheting damage exponentially higher than CS. In short, the TMS exhibits tunable, two-stage compression behavior and maintains good resilience under fatigue loading.

TMS enhanced bone regeneration

To further validate in vivo osteogenesis of TMS, we integrally designed and implanted the scaffolds for critical bone defects. Plates for screw fixation were incorporated with the scaffolds (Fig. S7). The geometry differences among CS, CS2 and TMS are the small gap (L_g) and pillar (d_p) as mentioned before. Thus, except the mechanical properties, the impact of other geometry factors on osteogenesis, such as pore size^{21,22}, curvature^{23,24}, and porosity⁹, can be neglected. We chose the ulnar bone of rabbits as the implantation site to utilize the adjacent tibia for support during the surgical procedure. This support helps

scaffolds securely in place without pre-tensioning and maintain their structural integrity²⁵.

Animal studies was conducted to validate the bone bridging through radiographic follow-up. The X-ray figures revealed a strong integration between the bone and scaffold interface (Fig. S8). No failure or concerning deformation of the scaffolds was observed in either group during 8-week period of implantation. The 3D reconstructed bone tissues were performed by micro-CT scanning (Fig. 3a). At 4 weeks, TMS exhibited substantial formation of new bone and higher bone density. The CS, on the other hand, formed a certain amount of new bone at the interface between the host bone and the implant. The TMS exhibited a 44% and 498% enhancement in the new bone fraction (BV/TV) (Fig. 3b) compared to the CS and CS2, respectively. Additionally, TMS exhibited a higher bone surface area fraction (BS/TV) (Fig. 3c). It is noteworthy that the CS structure exhibited the

formation of new bone at the outer edges of the scaffold, but did not achieve complete bridging across the entire structure in all duplicates. Conversely, the newly formed bone of the TMS exhibited a distinct bridge (Fig. S9). At 8 weeks, compact bone formation of high bone density was found in both groups with less cancellous tissue. The TMS demonstrated a bone reconstruction pattern comparable to host bone, with the new compact bone showing direct bridging to the upper and lower host bone. Whereas the CS failed to bridge the host bone and showed heterotopic ossification. As for CS2, among 8 implanted rabbits, one rabbit succumbed to a fracture infection at week 2, and two others developed ulnar fractures. The remaining rabbits failed to bridging the defects and exhibited typical radioulnar fusion, as illustrated in Fig. S10. Radioulnar fusion can restrict the range of motion in the arm and lead to functional deficits. Additionally, the micro-CT findings corresponded to histomorphology analysis in Fig. S11, showing a closed medullary cavity following CS2 implantation, resulting in the formation of a pseudoarticular joint. By comparing the compression of the three structures post-implantation, as shown in Fig. 3d, CS2 exhibited the highest compression deformation. Due to its low modulus, CS2 was insufficient to support bone loading, resulting in a deformation that exceeded the inflection point of TMS. Although the first-stage modulus of TMS is similar to that of CS2, the second-stage support of TMS can effectively restricted further compression deformation under higher loads. In short, both X-ray and micro-CT have shown the osteogenesis-enhancing ability of TMS compared with CS and CS2.

The osteogenesis of TMS was also validated through histological examination using Masson Goldner's trichrome staining on the central mid-sagittal plane of scaffolds. The staining results revealed the presence of immature orange osteoid and green mineralized new bone (Fig. 4a–p). At 4 weeks, all scaffolds remained intact. The quantity of newly formed bone in the center of the TMS group was significantly greater than that of the CS group (Fig. 4v). Additionally, the CS exhibited mineralized bone in the proximal and distal regions of the ulna, while the middle of the scaffolds contained a significant quantity of osteoid. In contrast, the TMS exhibited the formation of new bone within the central region of scaffold, which effectively bridges the ends of the ulna (Fig. 4a–f). Upon closer observation, it is evident that the new bone formation within the CS contains mainly mineralized tissue, with no notable cellular activity detected (Fig. 4g). Conversely, the TMS structure exhibits a greater number of nuclei within the newly formed bone, indicating the activity of ongoing bone regeneration (Fig. 4i). Besides, the osteoid in the CS displays unstructured morphology (Fig. 4h), while the TMS structure demonstrates a distinct orientation in the osteoid morphology that aligns with the direction of the loads (Fig. 4j). Following the extended 8-week period of implantation, both structures experienced substantial bone resorption and regeneration (Fig. 4k, l). Upon closer examination of the two structures in the same location, it was observed that the CS structure displayed a partial disconnection of new bone from the top of the scaffold, without complete bridging (Fig. 4m, n). The TMS structure, however, exhibited complete bridging of new bone from both ends and the mid of the scaffold (Fig. 4o, p).

The collagen fiber orientation was further examined through second-harmonic generation (SHG) (Fig. 4q, 4r and Fig. S12). Corresponding to the staining results of osteoid, the collagen fiber appeared to be more random of CS. Whereas in the TMS, the collagen showed a pronounced orientation parallel to the loads. Scanning electron microscopy (SEM) images depicted an active healing response (Fig. S13). At the vertical section of TMS after 4-week implantation (Fig. 4s), osseointegration new bone (light green) advancing through narrow pores of scaffolds (blue) could be observed. Microscopically, haversian-like system consist of surrounding osteocytes (dark green) and axial vasculature (red) was also seen (Figs. 4t and 4u), indicating bone regeneration from cancellous bone to compact bone and

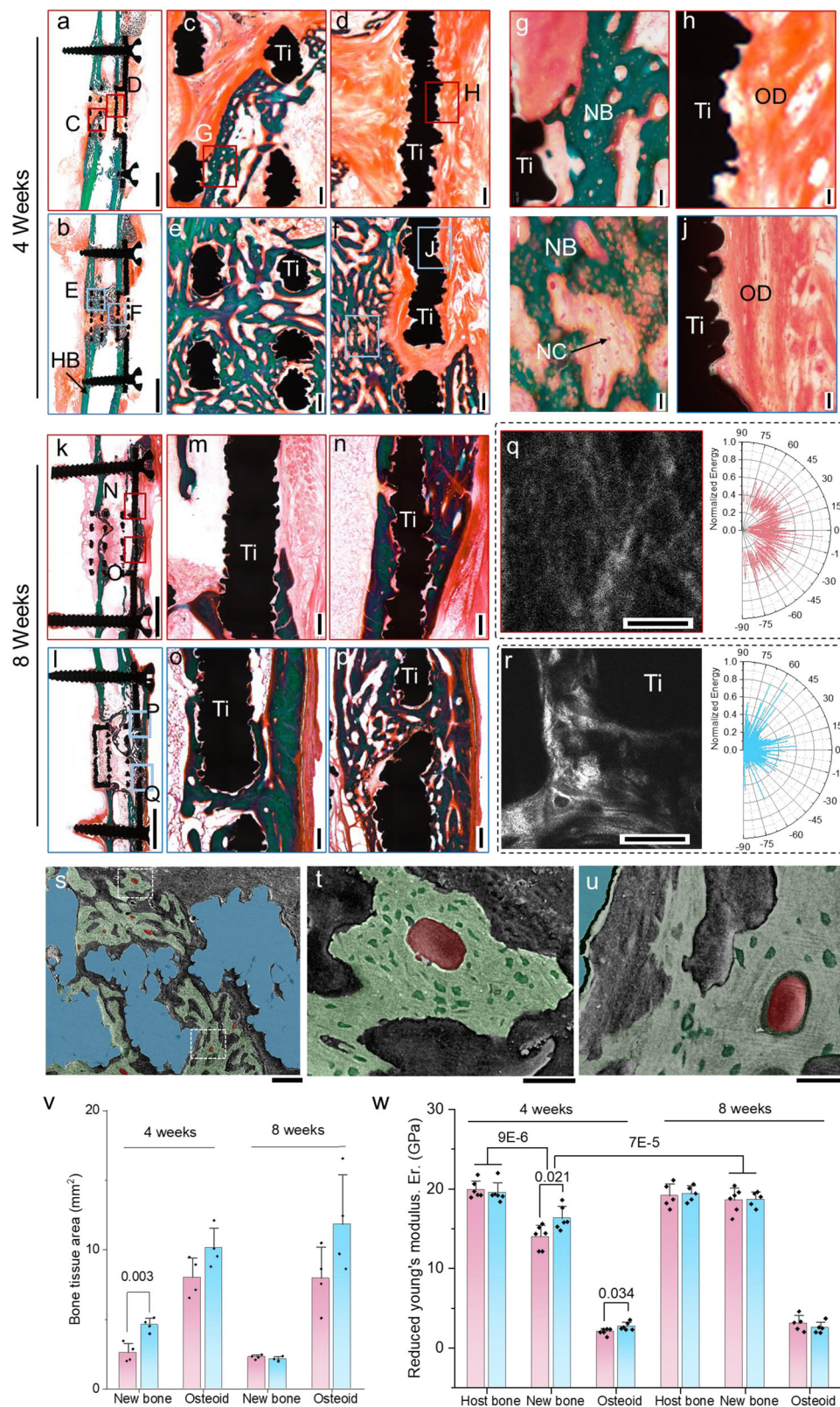
successful angiogenesis. The nanoindentation analysis of bone modulus at various locations revealed that the modulus of newly formed bone was significantly lower than that of the original bone at 4 weeks. Meanwhile, the modulus of the TMS was higher than that of CS for both new bone and osteoid. At 8 weeks, the new bone in both groups achieved a similar level of hardness as the host bone (Fig. 4w and Fig. S14), indicating the bone maturation.

Proteomic analysis

To comprehend the mechanism by which TMS stimulates bone formation, we collected newly formed bone from the scaffold after 4-week implantation. Subsequently, proteomic analysis and Western Blotting (WB) were conducted to identify the proteins and genes associated with bone formation that may be influenced by TMS (Fig. S15). Gene ontology (GO) analysis revealed that TMS is enriched in cellular components related to mechanical stimulation and cell migration (Fig. 5a). This leads to the activation of numerous calcium bindings, which can further promote the growth of skeletal muscle and bone. KEGG analysis of pathways showed that bone tissue of TMS react strongly to mechanical stimuli through focal adhesion and extracellular matrix (ECM). This process can subsequently activate the osteogenesis-related pathways such as AMPK and calcium signaling (Fig. 5b). The Volcano plot revealed that in the TMS group, 216 proteins were significantly up-regulated and 31 proteins were significantly down-regulated compared to the CS group (Fig. 5c). A subset of proteins associated with the bone regeneration process were plotted with heatmap (Fig. 5d). The levels of cellular force sensing and movement-related proteins, such as glycogen synthase 1 (GYS1) and phosphofructokinase (PFKM), were increased in TMS. The activation of key proteins, namely hypoxia inducible factor 1 subunit alpha (HIF-1 α), LDHA, ALDOA, and ENO1, provided strong evidence for the activation of HIF-1 α channels. Notably, western blot (Fig. 5e and Fig. S15e) confirmed a decrease in YAP proteins and an increase in classical osteogenic proteins of RUNX2 was also observed in TMS group. the HIF-1 α pathway of TMS group experiences substantial activation, indicating a potential increase in vascularization during bone regeneration. Therefore, TMS facilitates ECM deformation and mechano-biosensor of cells, thus promoting osteogenesis through activation of calcium ion channels. Meanwhile the intense cell deformation and proliferation can lead to localized hypoxia, hereby enhance angiogenesis through expression of HIF-1 α .

Discussion

After perceiving a mechanical stimulus, likely fluid stress in canaliculae or ECM deformation, a cascade of signaling events occurs in bone cells. Extensive research has focused on delineating cellular events, such as ion channel activity²⁶ and release of paracrine/autocrine factors²⁷. Currently, intensive studies of bone remodeling report the effects of external loads on mechanosensor and protein expressions, and still remains a topic of debate. In the context of critical bone defect reconstruction, the regulation of mechanical stimuli is evidently more complex and requires in-depth investigation across various stages of bone reconstruction. In the TMS group of this study, in addition to the activation of classical osteogenesis calcium ion channels and AMPK channels, we observed a significant upregulation of HIF-1 α . HIF-1 α can promote expression of Vascular endothelial growth factor (VEGF) thus enhance angiogenesis²⁸. Furthermore, there was a decrease in YAP expression observed both through proteomics analysis and Western blotting. YAP's translocation to the nucleus can be influenced by altering the rigidity of the biomaterial substrate on which the cells are cultured^{29,30}. However, its role in promoting osteogenesis remains a subject of controversy^{31–34}. Thus, the YAP channel remains one of mysteries in mechanical promotion of critical bone defect reconstruction and requires future researches. Fortunately, the tunable mechanical properties of TMS tackle the necessity to comprehend the



quantitative correlation of biomechanics for bone regeneration in the future.

We performed finite element modeling (FEM) to verify the strain behavior of bone tissue during osteogenesis (Fig. 6a, b). The calculations demonstrated that the interquartile range of the maximum principal strain in the CS callus tissue was between 0.4% and 1.1% (loading with twice the body weight, 2 BW), provided that the range

conductive to osteogenesis was attainable for CS. Nevertheless, this level of strain can only be attained under extreme conditions³⁵. Consequently, we conducted additional simulations to analyze the strain under lower loads. The CS scaffold exhibited a range of 0.2% to 0.6% at 50% of the maximum loads. At 25% of the maximum loads, the CS scaffolds exhibited strain values ranging from 0.1% to 0.3%, with an average strain below the threshold for bone formation. Thus, a certain

Fig. 4 | Histomorphological evaluations of the critical defect healing. Sections in the mid-sagittal plane are stained with the Masson-Goldner trichrome. The mineralized new bone (NB), osteoid (OD) and cell nucleus (NC) were stained green, orange and red, respectively. a, b 4 weeks after surgery. Scale bars = 5 mm. **c–f** Magnifications of **(a, b)** show the distinguished bone volume and growth direction. Scale bars = 300 μ m. **g–j** Magnifications of **(c–f)** show the microstructure of new bone growth frontiers and the orientation of the osteoid along the scaffold. Scale bars = 50 μ m. **k, l** 8 weeks after surgery. Scale bars = 5 mm. **m–p** Magnifications of **(k, l)** show bone tissue after reconstruction around the

scaffolds. Scale bars = 300 μ m. **q, r** SHG imaging and orientation map of collagen fiber at 4 weeks. Scale bars = 100 μ m. **s** vertical-section SEM images of TMS group showing the structural morphology of newly formed bone and its interaction scaffolds (blue). Scale bar = 100 μ m. **t, u** Osteocyte network and neovascularization (red, blood vessels) within haversian-like system and areas of new bone (light green, cancellous bone) and cells (dark green, osteocyte). Scale bar = 20 μ m **v** Bone tissue area calculated from histomorphology ($n = 4$). **w** Reduced young's modulus of bone tissues ($n = 5$) via nanoindentation tests. Data is represented as the mean \pm SD. p value of statistical significance is determined by two-tailed Student's t tests.

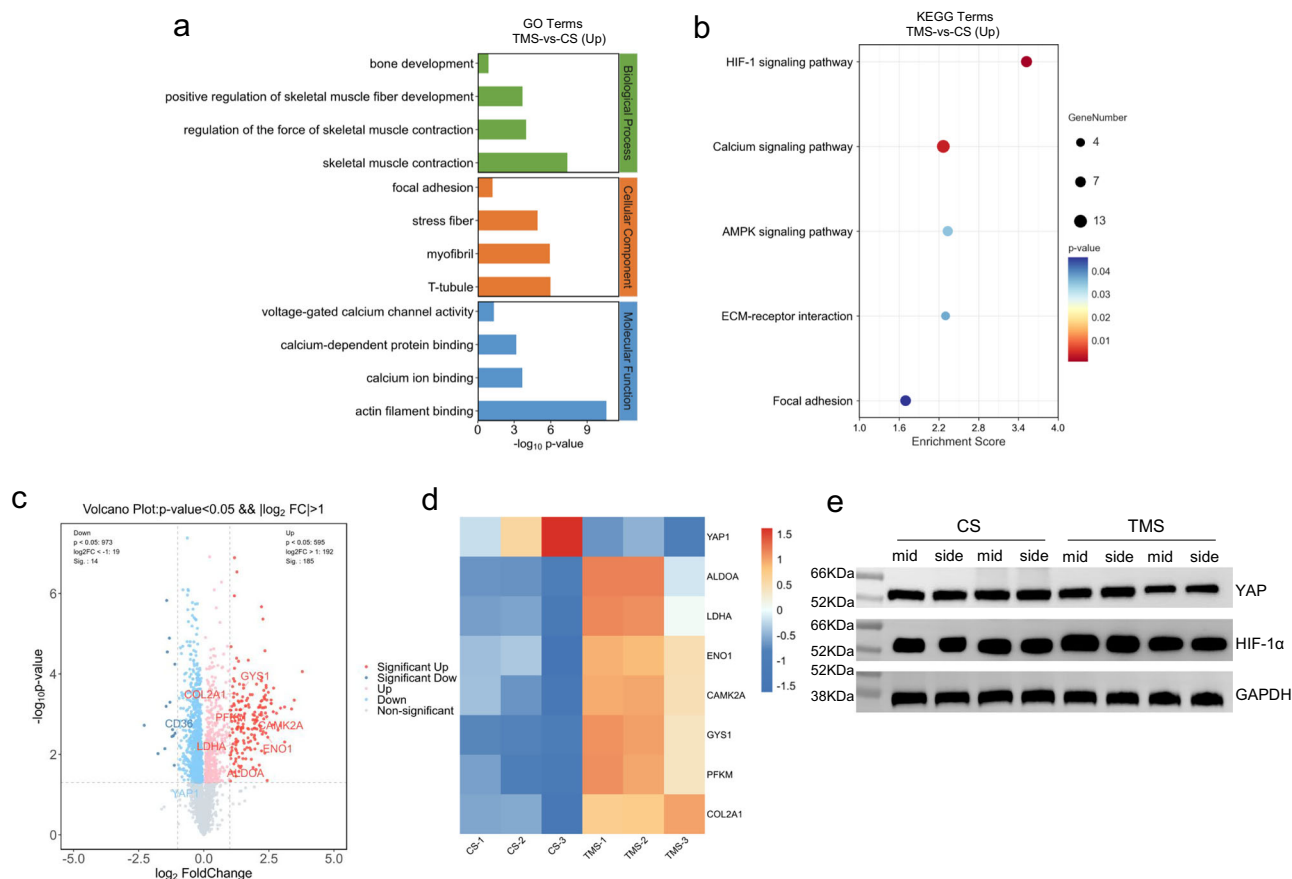


Fig. 5 | Proteomic analysis of bone regeneration. a GO terms with respect to biological process, cellular component and molecular function, and **b** KEGG pathway enrichment analyses. X-axis represents level of statistical significance of enrichment (Fisher exact test). **c** Volcano plot representation of differential abundance of protein. The x-axis indicates the differential expression profiles, plotting

the $\log_2(\text{FC})$. The y-axis indicates p-values by unpaired two-tailed t-test. **d** heatmap of differentially expressed proteins. ($n = 3$) **e** Selected protein levels measured with Western blot at the middle (mid) and side of the implants ($n = 4$). Exact p-values are available in the Source Data file.

level of strain shield occurs. In comparison, the TMS reached the 1.5%–4.2% range of straining under 2 BW load. A strain range of 1.3–3.3% and 1.2–3.1% was also presented when the loads were as low as 1 BW and 0.5 BW, respectively. The results indicate that the callus tissue strain of TMS is not sensitive to loads. When subjected to lower forces, TMS quickly enters the range of strain that triggers bone formation, thanks to its remarkably low effective modulus. Likewise, stronger forces activate a larger modulus of the TMS stiff stage, where the strains are less affected by the loads (Fig. 3h). By substituting the internal callus tissue with cartilage and cancellous bone material (Fig. 6d and Fig. S16). We found that as bone reconstruction process, TMS has the capacity to endure more than 4 times the strain than CS for bone development even filled with cartilage or cancellous bone.

When subjected to sustained forces, the strain experienced by the scaffold is contingent upon its effective modulus³⁶. The utilized implants targeting critical bone defects in reported research always

had a modulus above 100 MPa^{37–39}, where further reduction in modulus would result in insufficient strength. To delineate this constraint, we depicted strength normalized by effective modulus (σ/E_{eff})⁴⁰ in Fig. 6e. Historically, bulk metals, like Ti⁴¹, CoCr⁴², and Zn⁴³, were prevalent as implant materials. They approximately have a E_{eff} of 100 GPa and σ of 1000 MPa, resulting in $\sigma/E_{\text{eff}} \approx 0.01$. In the 21st century, advancements in 3D printing enabled the reduction of material moduli to approximately 100 MPa, meanwhile underscoring the imperative of strength: σ/E_{eff} gradually escalated to around 0.1^{11,21,44,45}. Further reduction in metal scaffold modulus necessitates mechanical metamaterial design and fabrication methodologies. For instance, a Ni metal scaffold can achieve a modulus of only 2 MPa with nanolattices⁴⁶. Nevertheless, even incorporating polymers⁴⁷, ceramics⁴⁸, and carbon⁴⁹, current mechanical metamaterials with one-stage deformation behaviors have σ/E_{eff} plateauing around 0.5. The notable trajectory of mechanical metamaterials such as ultra-

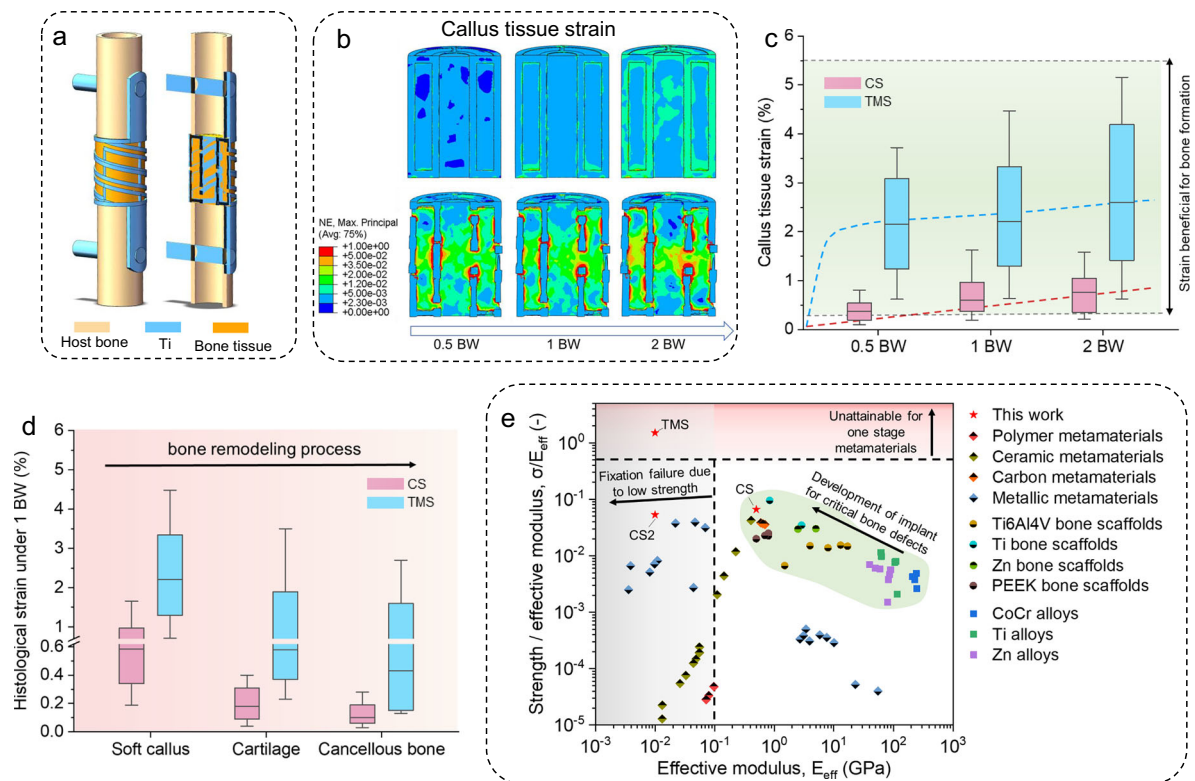


Fig. 6 | Bone tissue strain analysis and compressive properties of bone implants. **a** 3D finite element model (FEM) of the 6-mm ulnar defect with implantation of CS or TMS and augmented with a plate. **b** FEM analysis of maximum principal strains within the soft callus tissue and scaffolds under different body weight (BW) loading in the ROI. **c** FEM maximum principal strain values under varying load conditions with randomly selected grids, $n = 100$, whiskers extend to the 10–90% values, box represents the 25th to 75th percentiles, and centre represents mean value. **d** FEM maximum principal strain values of different bone tissues under 1 BW with randomly selected grids, $n = 25$, whiskers extend to the 10–90% values, box represents the 25th to 75th percentiles and centre represents mean

value. **e** Compressive properties of different metamaterials and bone implants. The plot is setup with strength normalized by the effective modulus vs. the effective modulus. The unattainable limit for one-stage metamaterial was plotted according to reference⁴⁰. Commercial bulk metals for bone implants, including Ti alloys⁴¹, CoCr alloys⁴², and biodegradable Zn alloys⁴³ are presented in solid squares. Bone scaffolds, including Ti6Al4V²⁰, Ti⁴⁴, biodegradable Zn¹¹ and polyetheretherketone (PEEK)⁴⁵ are labeled by circles with half-down interiors. Metamaterials, including metal⁴⁶, polymer⁴⁷, ceramics⁴⁸, and carbon⁴⁹ are labeled by diamonds with half-up interior.

stiffness⁵⁰ contrasts the requirements of bone implants. Consequently, the application of existing metamaterials to bone implants has not yielded significant results. Therefore, we propose the TMS possessing a two-stage deformation, which decouples the strength and modulus of the bone implant. An effective modulus of only 13.4 MPa was achieved, which is significantly lower than the limitations of current implants. Furthermore, the load-bearing requirements are satisfied in the stiff stage of TMS, which helps to obtain a σ/E_{eff} of 1.3.

While TMS exhibits promising performance in the ulna defects, there is a potential risk that it may only demonstrate the ductile stage behavior when subjected to tensile forces. Consequently, TMS may be more suitable for compression-dominated applications, such as interbody fusion devices. Still, compared with conventional scaffold design strategies of matching modulus to the bone, TMS opens a new scaffold design paradigm of generating sufficient strain of bone tissue to stimulate the regeneration. Above all, such concept can be applied to various materials, and is inherently independent of shape or loading direction. In the future, shape variations can be achieved by adjusting the shape of the TMS springs (e.g., polygons, ellipses). Moreover, two-stage deformation in other loading directions can be achieved by incorporating limit gaps, analogous to the compressive gap in TMS. The protocol of TMS transcends material-specific limitations and can be readily manufactured utilizing commercial 3D printing equipment, underscoring its versatility and accessibility within the fields of biomedical engineering.

Methods

Ethics

All experiments involving animals were conducted following protocols of the ARRIVE guidelines and approved by the Peking University Institutional Review Board on Biomedical Ethics in the Care and Use of Laboratory Animals (Project Number: LA20222326).

Materials and additive manufacturing

We fabricated the Ti6Al4V (Ti) scaffolds using an electron beam powder bed fusion (EBPBF) system (Q10plus, Arcam AB, Sweden). Typically, cylindrical CS and TMS scaffolds were converted into a standard triangulation language (STL) file and transferred to the EBPBF machine. The Ti powder (particle diameter: 45–100 μm , Arcam, Sweden)¹¹ was melted layer by layer according to the STL data and solidified by cooling afterward. The beam current was set as 28 mA. Scanning speed was 1200 mm/s. Linear energy was 1.4 J/mm. Slicing layer height is 0.05 mm. All prepared scaffolds were ultrasonically cleaned for 15 min in acetone, ethyl alcohol, and deionized water.

Mechanical tests and simulations

The quasi-static compression tests were carried out using a universal material testing machine (Instron 5969, USA) with a 100 kN load cell under room temperature. The loading rate was 0.5 mm/min, corresponding to an initial strain rate of 0.001/s according to ASTM E9-19. During compression tests, the strain of scaffolds was recorded using a digital image correlation (DIC) system (XTDIC-2D, China), see

Supplementary Movie 2. To ensure the reliability and reproducibility of the results, each sample was tested in triplicate.

Afterwards, the finite element modeling (FEM) of compression was conducted on a 32-core and 64-thread CPU (Intel Xeon Gold 6226 R Processor) using Abaqus/Explicit software (Dassault Corp, French). The FEM was based on two rigid load cell and deformable-implant-structure model to simulated the compression experiments⁴¹. The Ti material was set as homogeneous with a poisson ratio of 0.3. Young's modulus and yield strength of Ti were set as 116 GPa and 600 MPa, respectively. The simulated and experimental stress-strain curves are plotted in Fig. S17. In post-processing, the von-Mise stress under different strain was used to analyze the mechanical behaviors (Supplementary Movie 1).

Three-point bending tests were performed at room temperature using the same machine (Instron 5969, USA) with three replicates. In vivo implanted scaffolds were used for testing to closely mimics in vivo conditions. Two supports were added on the plates and the load was perpendicularly added to the axis of the scaffolds. The span length was set as 10 mm, and the cross-head speed was 0.5 mm/min.

Under compressively sinusoidal loading from 5 to 60 N (twice the body weight of the animal), fatigue tests were performed on an all-electric dynamic test instrument (Instron E3000, USA) with a frequency of 10 Hz with three replicates. The stress-controlled fatigue tests were performed until failure or until 1×10^6 cycles were reached.

Procedures of animal model establishment

Adult male New Zealand white rabbits (25 weeks, 3.0 ± 0.3 kg) were randomly assigned into 3 groups and subjected to surgery to create bone defects. The surgical procedures were performed with the rabbits under general anaesthesia using pentobarbital sodium (30 mg kg⁻¹, i.p.). Each rabbit's left anterior limb was fixed, shaved, and depilated. An incision around 30 mm was made parallel to the ulna. The muscles were then bluntly separated along the intermuscular space, exposing the middle part of the diaphysis. Using a pendulum saw, a bone defect approximately 10 mm in length at the middle part of the diaphysis was created as shown in Fig. S6b. The scaffold was implanted inside afterwards and fixed with two Ti6Al4V bone screws of 1.6 mm in diameter and 12 mm in length (Libeier, China) as shown in Fig. S6c. Animals were housed on a 12/12-h light/dark cycle, 21–25 °C, 40–70% humidity with adequate food and water. 4 weeks after surgery, 20 randomly selected rabbits were euthanised. 12 of them were used for radiographic analysis and histological analysis (4 rabbits from each group). 3 rabbits of CS and 3 rabbits of TMS were used for protein collection. 8 weeks after surgery, the rest of 12 rabbits were euthanized for radiographic analysis and histological analysis (4 rabbits from each group).

Radiographic analysis

X-ray images were performed at 0, 2, 4 and 6 weeks after surgery in all groups. Three specimens from each group were scanned by micro-CT (Siemens, Germany) at a scanning rate of 6 °/min and a resolution of 9 µm. The X-ray source voltage was 80 kV, and the beam current was 80 µA using filtered Bremsstrahlung radiation. The micro-CT DICOM images were then reconstructed using Mimics software (Mimics Medical 21.0, France). The bone was distinguished from soft tissue and titanium implants by partitioning different Hounsfield units (HUs). Firstly, the lowest and highest values of HUs were determined in the bone tissue region. Then the HU intervals of the bone tissue were divided and assign them to the heat map. The peripheral 2 mm region around and the intra-porous space within the implant were selected as the two regions of interest (ROI). In the ROI, the bone volume (BV) and bone volume/tissue volume (BV/TV) were calculated.

Histological preparation and evaluation

After 4 or 8 weeks, axial bone sections were prepared for histological analysis. The specimens were fixed in 10% formalin for 14 days and

dehydrated in serial ethanol concentrations (40%, 75%, 90%, 95%, and 100%) for three days. The specimens were then embedded in methyl methacrylate (MMA) and sectioned with an EXAKT power saw with a diamond blade (EXAKT Apparatebau, Germany). This system was then used to prepare ground sections of 40–50 µm, which were then stained with Masson-Goldner trichrome. A NanoZoomer digital slide scanner (Hamamatsu Photonics, Japan) was used to photograph the stained sections. The tissue sections were also examined under magnifications to determine the detailed tissue morphology. For SEM visualization, resin sections were also acid-etched with 37% phosphoric acid for 3 s and in 12.5% sodium hypochlorite for 5 min. Resin sections were then gold-sputtered at 20 mA for 140 s (Leica EM ACE600, Leica, Australia). An electron microscope (GeminiSEM, Zeiss, Germany) was used to image the resin sections using a high voltage of 15 kV at a constant 8.5 mm working distance.

Nanoindentation tests

Samples for nanoindentation studies were prepared with embedded ulnar cross-sections according to ISO 14577 standard. Before test, samples were grinded to 5000 grits and mechanically polished. Before testing, samples were ground to 5000 grit and mechanically polished. Nanoindentation (Bruker Hysitron TI980, Germany) tests were carried out using a standard Berkovich tip. A maximum load of 50 mN was applied longitudinally at a constant loading rate of 1.6 mN/s, following a holding time of 10 s. At least five indentations were made in the host bone, new bone, and osteoid areas of each specimen. In the selected tissue area, the indentations were arranged in a grid pattern with a spacing of 300 µm. The elastic behavior was verified by observing the load-displacement curves.

Second-harmonic generation imaging

SHG imaging was performed on MMA-embedded sections of the mid-sagittal plane in the CS and TMS groups to visualize collagen fiber orientation with a multidimensional confocal microfluorescence imaging system (ISS, USA). Two osteoid-rich regions were selected for each sample for SHG image capture. The SHG signal was generated with an 860 nm-wavelength laser. The SHG signal was detected in the range of 410 to 450 nm (that is, half-excitation wavelength). Images were recorded using a 40× objective with a scanning resolution of 512 × 512. The acquisition time of each image was set as 10 s. An open-access ImageJ plug-in, OrientationJ, was used to analyze the local anisotropy of collagen fibrils in SHG images⁵¹. OrientationJ was connected to a macro that carried out orientation analysis within several 10 × 10-pixel sub-ROIs that covered the overview image in a grid-like pattern with finite difference gradient method. The primary fiber orientation was visualized as a yellow line in each sub-ROI with a scale factor of 150% and normalized energy (defined as the trace of the structure tensor matrix). The length of the line indicates the degree of anisotropy. Normalized energy and angles was also plotted to show the fiber orientation.

Tissue strain analysis

In order to determine the deformation behavior within the bone tissue when the scaffolds were implanted into the defect site, a finite element model including the ulnar bone, Ti scaffolds, and two screws was developed. In addition, the scaffold pores and medullary canal were filled with a soft callus material to simulate the magnitude of strain within the healing region during early osteogenesis. The callus material was also replaced with cartilage and cancellous bone (Supplementary Fig. S15) to simulate tissue strain after bone filling. In this model, a combined static load of axial compression and anterior-posterior bending was added to the upper face of the host bone. And the lower host bone was fixed. The magnitude of axial loading was set at 15, 30 or 60 N, which corresponded to half to twice the average body weight of the animal (3 kg) under different posture conditions. The bending moment was therefore calculated based on the angle of the rabbit ulna

bone to the vertical (approximately 15 degrees), reaching a maximum moment of 0.16 N·m. The surfaces of the scaffold and bone tissue were modeled with tie-constraints to simulate their physical interaction in Abaqus/Explicit. The scaffold is The Ti scaffolds and screws had a Young's modulus of 116 GPa with a Poisson's ratio of 0.30; the host bone had a Young's modulus of 17 GPa with a Poisson's ratio of 0.30; the soft callus tissue had a Young's modulus of 0.2 MPa and a Poisson's ratio of 0.167; the cartilage had a Young's modulus of 1 MPa and a Poisson's ratio of 0.4; the cancellous bone had a modulus of 300 MPa with a Poisson's ratio of 0.3.

Proteomics analysis

The new bone tissues of three specimens from each group were carefully separated right after sacrifice and immediately frozen by liquid nitrogen. After thorough grinding, the phenol extraction method was applied for protein extraction. Specifically, phenol extract was prepared by adding 2.4 g sucrose (Hushi, China), 0.058 g NaCl (Sangong Biotech, China), 0.146 g EDTA-2Na (Solarbio, China), 0.02 g DTT (Solarbio, China), 2.5 mL 0.5 M Tris-HCl (pH 6.8, Sangong Biotech, China), 2.5 mL 1.5 M Tris-HCl (pH 8.8, Sangong Biotech, China) and adjusting the volume with ddH₂O to 10 mL. Then an equal volume of phenol-Tris-HCl (pH 7.8, Sangong Biotech, China) saturated solution was added and mixed at 4 °C for 40 min. After collection of the upper phenol phase through centrifugation, five times the volume of pre-chilled 0.1 M ammonium acetate-methanol solution (Sangong Biotech, China) was added and precipitated for 24 h at −40 °C. Precipitates were then collected and washed with pre-chilled methanol and acetone, respectively. Then precipitates were dissolved in lysis buffer at room temperature for 3–5 min. Centrifuge the solution to collect the supernatant, which is the total protein solution of the sample. The proteomics sequencing and analysis were conducted by OE Biotech Co., Ltd., China. After the significance analysis, differentially expressed genes were selected for volcano and heatmap plots according to certain criteria (p-value < 0.05 and fold change > 2). Gene ontology (GO) and Kyoto Encyclopedia of Genes and Genomes (KEGG) pathway enrichment analyses by OECloud Tools.

Western blot assay

In the Western blot test, two rabbits were selected from each group of TMS and CS, and bone tissue was collected from both the middle and the side of the scaffold for each rabbit. Proteins (30 µg /lane) were separated using the same methods as the proteomics test. The primary antibodies, including anti-YAP1 (abs131839, Absin, China), anti-Runx2 (AV36678, Sigma, USA), anti-COL2A (abs120144, Absin, China), anti-HIF-1α (NB100-105, Novus, China), and anti-GAPDH (abs137959, Absin, China) were purchased commercially. Protein bands were photographed using an ImageQuant LAS500 imager (GE, Marlborough, MA, USA).

Statistical analysis

The numerical data were analyzed using Origin 2019b (OriginLab, Northampton MA, USA). Two-tailed test was used to determine significant differences between two groups. One-way ANOVA followed by Tukey's post hoc multiple comparison test. Data are presented as mean ± SD ($n \geq 3$, independent samples). Besides, Ontologies included GO and KEGG were selected based on enrichment scores, with a Fisher test p -value of < 0.05.

Reporting summary

Further information on research design is available in the Nature Portfolio Reporting Summary linked to this article.

Data availability

All data supporting the findings of this study are available within the article and its supplementary files. Any additional requests for information can be directed to, and will be fulfilled by, the corresponding

authors. The 3D files of TMS, CS and CS2 are publicly available in the GitHub repository at <https://github.com/youqinpk/A-Metamaterial-Scaffold>. Source data are provided with this paper.

References

- Nauth, A., Schemitsch, E., Norris, B., Nollin, Z. & Watson, J. T. Critical-Size Bone Defects: Is There a Consensus for Diagnosis and Treatment? *J. Orthop. Trauma* **32**, S7–S11 (2018).
- Wang, X. et al. Topological design and additive manufacturing of porous metals for bone scaffolds and orthopaedic implants: A review. *Biomaterials* **83**, 127–141 (2016).
- Wolff, J. The Classic: On the Inner Architecture of Bones and its Importance for Bone Growth. *Clin. Orthop. Relat. Res.* **468**, 1056–1065 (2010).
- Sparks, D. S. et al. Convergence of scaffold-guided bone regeneration principles and microvascular tissue transfer surgery. *Sci. Adv.* **9**, eadd6071 (2023).
- Smit, T., Koppen, S., Ferguson, S. J. & Helgason, B. Conceptual design of compliant bone scaffolds by full-scale topology optimization. *J. Mech. Behav. Biomed. Mater.* **143**, 105886 (2023).
- Pobloth, A.-M. et al. Mechanobiologically optimized 3D titanium-mesh scaffolds enhance bone regeneration in critical segmental defects in sheep. *Sci. Transl. Med.* **10**, eaam8828 (2018).
- Shefelbine, S. J., Augat, P., Claes, L. & Simon, U. Trabecular bone fracture healing simulation with finite element analysis and fuzzy logic. *J. Biomech.* **38**, 2440–2450 (2005).
- Lacroix, D. & Prendergast, P. J. A mechano-regulation model for tissue differentiation during fracture healing: analysis of gap size and loading. *J. Biomech.* **35**, 1163–1171 (2002).
- Kelly, C. N. et al. High-strength, porous additively manufactured implants with optimized mechanical osseointegration. *Biomaterials* **279**, 121206 (2021).
- Mastrogiacomo, M. et al. Tissue engineering of bone: search for a better scaffold. *Orthod. Craniofacial Res.* **8**, 277–284 (2005).
- Peng, B. et al. Machine learning-enabled constrained multi-objective design of architected materials. *Nat. Commun.* **14**, 6630 (2023).
- Stráský, J. et al. Achieving high strength and low elastic modulus in interstitial biomedical Ti–Nb–Zr–O alloys through compositional optimization. *Mater. Sci. Eng.: A* **839**, 142833 (2022).
- Meeussen, A. S. & van Heck, M. Multistable sheets with rewritable patterns for switchable shape-morphing. *Nature* **621**, 516–520 (2023).
- Frenzel, T., Kadic, M. & Wegener, M. Three-dimensional mechanical metamaterials with a twist. *Science* **358**, 1072–1074 (2017).
- Dagdelen, J., Montoya, J., de Jong, M. & Persson, K. Computational prediction of new auxetic materials. *Nat. Commun.* **8**, 323 (2017).
- Sun, M., Hu, X., Tian, L., Yang, X. & Min, L. Auxetic Biomedical Metamaterials for Orthopedic Surgery Applications: A Comprehensive Review. *Orthop. Surg.* **16**, 1801–1815 (2024).
- Fan, J. et al. A review of additive manufacturing of metamaterials and developing trends. *Mater. Today* **50**, 303–328 (2021).
- Barri, K. et al. Patient-Specific Self-Powered Metamaterial Implants for Detecting Bone Healing Progress. *Adv. Funct. Mater.* **32**, 2203533 (2022).
- Wang, L. et al. In vitro fatigue behavior and in vivo osseointegration of the auxetic porous bone screw. *Acta Biomaterialia* **170**, 185–201 (2023).
- Song, C. et al. Research progress on the design and performance of porous titanium alloy bone implants. *J. Mater. Res. Technol.* **23**, 2626–2641 (2023).
- Chen, Z. et al. Influence of the pore size and porosity of selective laser melted Ti6Al4V ELI porous scaffold on cell proliferation, osteogenesis and bone ingrowth. *Mater. Sci. Eng.: C* **106**, 110289 (2020).

22. Taniguchi, N. et al. Effect of pore size on bone ingrowth into porous titanium implants fabricated by additive manufacturing: An in vivo experiment. *Mater. Sci. Eng. C* **59**, 690–701 (2016).
23. Callens, S. J. P. et al. Emergent collective organization of bone cells in complex curvature fields. *Nat. Commun.* **14**, 855 (2023).
24. Ehrig, S. et al. Surface tension determines tissue shape and growth kinetics. *Sci. Adv.* **5**, eaav9394 (2019).
25. Zhang, Z. et al. Biodegradable ZnLiCa ternary alloys for critical-sized bone defect regeneration at load-bearing sites: In vitro and in vivo studies. *Bioact. Mater.* **6**, 3999–4013 (2021).
26. Wang, L. et al. Mechanical sensing protein PIEZO1 regulates bone homeostasis via osteoblast-osteoclast crosstalk. *Nat. Commun.* **11**, 282 (2020).
27. Duda, G. N. et al. Analysis of inter-fragmentary movement as a function of musculoskeletal loading conditions in sheep. *J. Biomech.* **31**, 201–210 (1997).
28. Hu, K. et al. Hypoxia-inducible factor 1 upregulation of both VEGF and ANGPTL4 is required to promote the angiogenic phenotype in uveal melanoma. *Oncotarget* **7**, No 7 (2016).
29. Li, W. et al. Mst1/2 Kinases Modulate Glucose Uptake for Osteoblast Differentiation and Bone Formation. *J. Bone Miner. Res.* **33**, 1183–1195 (2018).
30. Lin, X. et al. AP2a enhanced the osteogenic differentiation of mesenchymal stem cells by inhibiting the formation of YAP/RUNX2 complex and BAX1 transcription. *Cell Prolif.* **52**, e12522 (2019).
31. Caliri, S. R., Vega, S. L., Kwon, M., Soulas, E. M. & Burdick, J. A. Dimensionality and spreading influence MSC YAP/TAZ signaling in hydrogel environments. *Biomaterials* **103**, 314–323 (2016).
32. Elosaegui-Artola, A. et al. Force Triggers YAP Nuclear Entry by Regulating Transport across Nuclear Pores. *Cell* **171**, 1397–1410.e14 (2017).
33. Vermeulen, S., Tahmasebi Birgani, Z. & Habibovic, P. Biomaterial-induced pathway modulation for bone regeneration. *Biomaterials* **283**, 121431 (2022).
34. Wang, H., Yu, H., Huang, T., Wang, B. & Xiang, L. Hippo-YAP/TAZ signaling in osteogenesis and macrophage polarization: Therapeutic implications in bone defect repair. *Genes Dis.* **10**, 2528–2539 (2023).
35. Duda, G. N. et al. The decisive early phase of bone regeneration. *Nat. Rev. Rheumatol.* **19**, 78–95 (2023).
36. Qin, Y. et al. Processing optimization, mechanical properties, corrosion behavior and cytocompatibility of additively manufactured Zn-0.7Li biodegradable metals. *Acta Biomaterialia* **142**, 388–401 (2022).
37. Li, Y. et al. 3D printing titanium grid scaffold facilitates osteogenesis in mandibular segmental defects. *npj Regenerative Med.* **8**, 38 (2023).
38. Qin, Y. et al. Additive manufacturing of Zn-Mg alloy porous scaffolds with enhanced osseointegration: In vitro and in vivo studies. *Acta Biomaterialia* **145**, 403–415 (2022).
39. Huang, X. et al. Biomaterial scaffolds in maxillofacial bone tissue engineering: A review of recent advances. *Bioact. Mater.* **33**, 129–156 (2024).
40. Bauer, J. et al. Nanolattices: An Emerging Class of Mechanical Metamaterials. *Adv. Mater.* **29**, 1701850 (2017).
41. Tshephe, T. S., Akinwamide, S. O., Olevsky, E. & Olubambi, P. A. Additive manufacturing of titanium-based alloys- A review of methods, properties, challenges, and prospects. *Heliyon* **8**, e09041 (2022).
42. Zhou, Y., Li, N., Yan, J. & Zeng, Q. Comparative analysis of the microstructures and mechanical properties of Co-Cr dental alloys fabricated by different methods. *J. Prosthet. Dent.* **120**, 617–623 (2018).
43. Qin, Y. et al. Additive manufacturing of biodegradable metals: Current research status and future perspectives. *Acta Biomaterialia* **98**, 3–22 (2019).
44. Zhang, M. et al. 3D printing of Haversian bone-mimicking scaffolds for multicellular delivery in bone regeneration. *Sci. Adv.* **6**, eaaz6725 (2020).
45. Yuan, B. et al. A biomimetically hierarchical polyetherketoneketone scaffold for osteoporotic bone repair. *Sci. Adv.* **6**, eabc4704 (2020).
46. Zheng, X. et al. Multiscale metallic metamaterials. *Nat. Mater.* **15**, 1100–1106 (2016).
47. Zheng, X. et al. Ultralight, ultrastiff mechanical metamaterials. *Science* **344**, 1373–1377 (2014).
48. Meza, L. R., Das, S. & Greer, J. R. Strong, lightweight, and recoverable three-dimensional ceramic nanolattices. *Science* **345**, 1322–1326 (2014).
49. Crook, C. et al. Plate-nanolattices at the theoretical limit of stiffness and strength. *Nat. Commun.* **11**, 1579 (2020).
50. Jiao, P. et al. Mechanical metamaterials and beyond. *Nat. Commun.* **14**, 6004 (2023).
51. Rezakhanlou, R. et al. Experimental investigation of collagen waviness and orientation in the arterial adventitia using confocal laser scanning microscopy. *Biomech. Modeling Mechanobiol.* **11**, 461–473 (2012).

Acknowledgements

The authors sincerely thank Dr Chongbin Wei from AKMedical Corp. China for the support of 3D printing. Funding support was provided from National Natural Science Foundation of China 52301302 (Y.Q.), 82302684 (Z.J.), 5231101024 (Y.Z.), U22A20121 (Y.Z.). Beijing Natural Science Foundation L244002 (W.L.). National Key Research and Development Program of China 2023YFC3604400 (W.L.). Guangdong Basic and Applied Basic Research Foundation 2024A151012042 (Y.Q.). China Postdoctoral Science Foundation 2023M732339 (Y.Q.), 2024T170576 (Y.Q.).

Author contributions

Conceptualization: Y.Q.; Methodology: Y.Q., Z.J., Y.W.; Investigation: Y.Q., Z.J., D.Z., H.Y., K.C.; Visualization: Y.Q., Z.J. Funding acquisition: Y.Q., Z.J., W.L., Y.Z.; Project administration: W.L., Y.Z. Supervision: W.L., P.W., Y.Z. Writing – original draft: Y.Q., Z.J. Writing – review & editing: W.L., P.W., Y.Z.

Competing interests

The authors declare no competing interests.

Additional information

Supplementary information The online version contains supplementary material available at <https://doi.org/10.1038/s41467-025-57609-9>.

Correspondence and requests for materials should be addressed to Weishi Li, Peng Wen or Yufeng Zheng.

Peer review information *Nature Communications* thanks Seung Yun Nam, who co-reviewed with Masoud Shirzad, Frederik Claeysens and the other, anonymous, reviewer(s) for their contribution to the peer review of this work. A peer review file is available.

Reprints and permissions information is available at <http://www.nature.com/reprints>

Publisher's note Springer Nature remains neutral with regard to jurisdictional claims in published maps and institutional affiliations.

Open Access This article is licensed under a Creative Commons Attribution-NonCommercial-NoDerivatives 4.0 International License, which permits any non-commercial use, sharing, distribution and reproduction in any medium or format, as long as you give appropriate credit to the original author(s) and the source, provide a link to the Creative Commons licence, and indicate if you modified the licensed material. You do not have permission under this licence to share adapted material derived from this article or parts of it. The images or other third party material in this article are included in the article's Creative Commons licence, unless indicated otherwise in a credit line to the material. If material is not included in the article's Creative Commons licence and your intended use is not permitted by statutory regulation or exceeds the permitted use, you will need to obtain permission directly from the copyright holder. To view a copy of this licence, visit <http://creativecommons.org/licenses/by-nc-nd/4.0/>.

© The Author(s) 2025